Materials Horizons

ROYAL SOCIETY OF CHEMISTRY

COMMUNICATION

View Article Online
View Journal | View Issue

Cite this: *Mater. Horiz.*, 2025, 12, 899

Received 6th September 2024,
Accepted 4th November 2024

DOI: 10.1039/d4mh01220h

rsc.li/materials-horizons

Reduction-immobilizing strategy of polymer-embedded sub-2 nm Cu nanoparticles with uniform size and distribution responsible for robust catalytic reactions†

Rosy Amalia Kurnia Putri,[a] Wail Al Zoubi,*[b] Bassem Assfour,[c] Abdul Wahab Allaf,[cd] Sudiyarmanto[a] and Young Gun Ko*[b]

Polymer-embedded metal nanoparticles are in great demand owing to their unique features, leading to their use in various important applications, including catalysis reactions. However, particle sintering and aggregation are serious drawbacks, resulting in a drastic loss of catalytic activity and recyclability. Herein, a reduction-immobilizing strategy of polymer-embedded sub-2 nm Cu nanoparticles offered highly controlled distribution and nanoparticle size within polymer structures with high fidelity. This work sheds light on the high catalytic performance of nanoparticles that rely on their ultrasmall size and uniform distribution in polymer structures, generating more active sites that result in high efficiency reduction of organic compounds. A catalysis study was carried out for the hydrogenation of nitro compounds, achieving nearly 100% reduction in an extremely short time and remaining stable after 15 consecutive cycles. Furthermore, the catalytic mechanism was demonstrated by density functional theory (DFT) calculations. Notably, the discovery of this facile strategy may enable the remarkable cutting-edge design of catalyst materials with promising performance and stability.

New concepts

We put forward the catalytic performance of hybrid materials consisting of polymer-embedded Cu nanoparticles (NPs) on top of an inorganic layer fabricated by plasma electrolysis, with a special highlight on the uniform size and distribution of Cu NPs, leading to robust catalytic performance. The interaction between polymer-Cu NPs-inorganic layer was calculated *via* computational simulation and the proposed catalytic mechanism was discussed to provide more insight on how this material might be considered as an efficient candidate for catalytic applications.

1. Introduction

Noble metal nanoparticles (NPs) belong to an important class of materials owing to their great physiochemical properties and particular electronic structure as well as their state-of-the-art applications in many fields, especially in plasmonics,[1] optics,[2] catalysis, photocatalysis, and electrocatalysis.[3–9] In particular, ultra-small size nanoparticles demonstrate high activity in the related applications.[10–13] However, upon efficient utilization at the industrial level, such as the effective transformation of organic compounds into high added-value components, the high cost of Pt,[14] Ag,2 and Pd[15,16] is prohibitive. Therefore, the ever-growing demand for industrial applications has boosted the exploration of alternative materials that are both cost-effective and highly active. For decades, Cu-NPs have been particularly attractive due to their low cost and high natural abundance while offering comparable thermal and electrical conductivity.[17] However, the inherent instability of Cu-NPs under atmospheric conditions often leads to high susceptibility to oxidation in the air, allowing the formation of more stable copper oxide NPs, which hinders their structural integrity as well as the potential for the aforementioned applications.

Apparently, numerous approaches for synthesizing Cu-NPs generally rely on conventional chemical treatments, such as microwave-assisted methods,[18] electrochemical synthesis,[19] and wet-chemical methods.[20] Despite specific successful efforts and noteworthy progress in these methods, the use of Cu-NPs is still restricted by the long-lasting problems that arise from (i) the high intrinsic tendency of NPs to aggregate and (ii) inherent instability under atmospheric conditions, and thus ought to be kept as a suspension at ultralow temperature. Nonetheless,

[a] *Research Center for Chemistry, National Research and Innovation Agency-BRIN, Building 452, KST BJ Habibie, Tangerang Selatan, Banten 15314, Indonesia*
[b] *Materials Electrochemistry Group, School of Materials Science and Engineering, Yeungnam University, Gyeongsan 38541, South Korea. E-mail: wailalzoubi@ynu.ac.kr, younggun@ynu.ac.kr*
[c] *Atomic Energy Commission, Department of Chemistry, P.O. Box 6091, Damascus, Syria*
[d] *Arab International University, Department of Pharmaceutical Chemistry and Quality Control, Faculty of Pharmacy, Ghabaghib, Darra, Syria*

† Electronic supplementary information (ESI) available. See DOI: https://doi.org/10.1039/d4mh01220h

freeze drying the suspension of NPs typically results in the irreversible aggregation of NPs, which are unlikely to be redispersed.[21] To address these issues, researchers have developed metal supports in which various methods have been proposed to improve the chemical stability of Cu-NPs, especially in aqueous solution, by utilizing polymer ligands such as polyethylene glycol,[22] polystyrene,[23] and polyacrylamide.[24] For instance, Poupart and coworkers[25] developed the use of a permeable monolith as a support for Cu-NPs. The presynthesis method involved three steps: synthesis of the monolithic capillaries and surface pretreatment of the monolith, *in situ* synthesis of the porous monolith, surface functionalization, and eventually *in situ* formation of copper nanoparticles. For the same purpose, Zhang *et al.*[26] fabricated and immobilized Ag–Cu NPs on the surface of polypropylene fabrics to prevent agglomeration by combining a radiation-induced grafting method with postprocessing. Another report by Haider *et al.*[27] synthesized Cu-NPs/CS-CMM (chitosan-cellulose microfiber mat) by adhering CS on CMM and adsorbing Cu^{2+} ions, followed by chemical reduction of ions to Cu-NPs. Sun and coworkers prepared Cu-NPs/Cu_xO/C by a wet chemical method on MOF-based foam by the *in situ* growth of carboxymethyl cellulose (CMC), followed by pyrolysis of the two synthesized precursors at 600 °C.[28] Lichen Wang *et al.* successfully carried out the immobilization of nano-Cu on a ceramic membrane, resulting in more uniformly dispersed Cu nanoparticles which provided more active sites for the catalytic reaction, leading to enhanced catalytic conversion.[29] Different approaches were employed primarily by introducing additional capping agents to stabilize Cu-NP nanoparticles, as demonstrated by Verma *et al*.[30] They fabricated Cu-NPs with polyvinyl pyrrolidone (PVP) to generate stable materials because Cu–polymer composites, at least two major components, have the potential to outperform similar materials made from any one of their single components. However, practical application of supported Cu catalysts of the aforementioned synthesis methods faces great challenges as follows: (i) the requirement of high-temperature reactions that are not preferable in industrial fields; (ii) uncontrollable and inhomogeneous Cu particle growth in size and distribution; (iii) the challenges of fabricating polymer-supported Cu-NPs with small metal sizes and superior stability by one step; (iv) the recovery process of Cu-NPs from an aqueous solution often being time-consuming and complex; (v) the poor stability of Cu-NPs, which tend to sinter easily under reaction, leading to a drastic loss of their catalytic activity with time; (vi) apparent hydrolysis of the polymer in aqueous solutions. In addition to that, the recovery of nanoparticle-polymer catalysts from aqueous solution still remains a serious problem to be solved and contributes to a drastic loss of catalytic activity with time. Therefore, it remains a critical challenge to create an effective and general route for preparing supported Cu-NPs with both excellent catalytic activity and long-term stability under extreme environmental conditions.

In this research work, the authors have successfully fabricated a layer-by-layer catalyst material comprising Cu NPs supported on a polymer matrix, which is anchored on MgO by taking advantages of the naturally formed porous surface. This research work has successfully addressed several challenges identified in the previous studies, such as the attempt to achieve uniform size and distribution which strongly influence the catalytic performance of 4-NP reduction. These issues remain critical challenges using conventional synthetic techniques.[31–33] In this work, the synthesis of Cu NPs occurred at a temperature comparatively lower than that of other methods,[33–35] which is more preferable to be applied in the industrial field due to its ease of use, simplicity, and real-time aspects. Moreover, Cu NPs grew uniformly both at particularly small size and uniform distribution due to the encapsulation of the polymer layer, enhancing overall catalytic performance. Unlike conventional Cu NPs in the form of a powder, Cu-PVAc@MgO offered a direct and efficient recovery process, reducing the time and complexity of catalyst recovery. In addition, the growth of the Cu NPs on the polymer matrix, which is anchored on porous MgO, maintains constant activity over extended cycles, avoiding unnecessary active site leaching as well as NP sintering that may significantly reduce the catalytic performance. Eventually, the presence of MgO ensured the structural stability of the Cu-containing PVA layer and prevented the degradation and deactivation. Thus, we proposed a new method, a reduction-immobilizing strategy (R-IS), and succeeded in embedding sub-2 nm Cu-NPs in a polymer layer anchored onto porous MgO. R-IS is a method comprising a plasma-assisted process to produce a porous MgO film that can provide specific adsorption sites for stabilizing polyvinyl acetate (PVAc)-supported Cu-NPs, thereby maintaining catalytic performance. These unique porous structures of MgO not only merge the features of active site availability but also donate vast space for the nucleation and incorporation of various organic polymers or catalytically active species, including polymers, metal organic frameworks (MOFs) or M-NPs (*e.g.*, Au, Pd, Ru, Rh, Cu, Ni, Fe).

Herein, the porous MgO layer was used as a catalyst support to load the Cu-NPs generated from the *in situ* reduction of a metal salt ($Cu(NO_3)_2$) in the presence of polyvinyl acetate (PVAc) as a polymeric stabilizer of Cu-NPs to prevent the oxidation and aggregation of Cu-NPs, which is of upmost importance for the catalytic performance. The robust and direct immobilization of PVAc-embedded Cu-NPs on the porous surface would result in completely adhered Cu-NPs to the surface of the porous MgO support. Hence, PVAc-embedded Cu-NPs are utilized to improve the catalytic reduction of 4-nitrophenol (4-NP) as a toxic environmental pollutant that poses a great threat to human health and remains in the environment for a long period due to its stability, into non-hazardous compounds such as 4-aminophenol (4-AP), thereby removing the toxic material and preparing high-value chemicals,[36] which is an essential intermediate in the preparation of explosives, organic pigments, pesticides, and medicines.[37] As a result, an outstanding synergistic effect between polymer-Cu-NPs and MgO support is expected, as further clarified by density functional theory (DFT), giving rise to new structural integrity and adding to the

versatility of catalytic properties, which opens new opportunities for the robust advancement of the catalysis field.

2. Results and discussion

2.1. Structural analysis of uniformly dispersed Cu-NPs embedded in PVAc on an MgO support

Conventionally, recent approaches (*e.g.*, three complementary strategies: *in situ* growth of M-NPs, integration of M-NPs into resin surfaces, and selective surface decoration of polymeric structures) have been widely implemented to fabricate a large number of M-NP-polymer catalysts using wet chemical methods; however, these strategies require sophisticated and challenging preparation processes as well as cost-ineffective processes with limited control of NP size and size distribution.[38] In contrast, the proposed system of ''R-IS'' contains two steps: (1) facile and simultaneous reduction of metal precursors and assembly of the polymer shell surrounding the reduced metal NPs and (2) anchoring of the metal-polymer onto the porous MgO fabricated using a reduction-assisted method. As a demonstration, we synthesized Cu NPs embedded by crosslinked PVAc (citric acid (CA) as a cross-linking agent) anchored onto a porous MgO support layer grown on a Mg plate, denoted as Cu-PVAc@MgO, as illustrated in Fig. 1a. By taking advantage of physical bonding between the Cu-PVAc layer and MgO layer through interconnected pores, cracks and defects, the surface roughness of the MgO layer can significantly enhance the contact area and offer multiple anchoring points through mechanical interlocking with the polymer. This would influence the dispersion and adhesion of the Cu-PVAc layer, hence improving the stability of the Cu-PVAc layer. In addition, intermolecular interactions such as van der Waals forces and hydrogen bonding are expected to contribute to the successful adherence of Cu-PVAc on the MgO layer. Notably, porous MgO film supports are generated by the PE method (Fig. S1, ESI†), resulting from the unique electrical field effect (described in the Supplementary Note and Fig. S2, ESI†), which is generally used in the surface treatment of light practical metals (*i.e.*, Mg-, Al-, and Ti-alloys).[39,40] The SEM cross-sectional morphology of Cu-PVAc@MgO is displayed with additional information for each layer in Fig. S3 (ESI†).

Apparently, the uniform microstructure generated by R-IS was shown by the low-magnification TEM in Fig. 1a. The size and distribution of Cu-NPs are depicted in Fig. 1b as well as Fig. S4 (ESI†), showing comparatively high-magnification images where Cu-NPs are clearly visible and embedded in the amorphous polymer matrix at which varied ultrasmall NP sizes are mostly approximately 1–2 nm. The illustration in the inset of Fig. 1c depicts how Cu-NPs were embedded by a polymer in which the blue line describes the polymer chains, while the purple line in the dashed line illustrates the cross-linking agent, citric acid (CA). In this case, CA would strengthen one polymer chain to the other chain as a result of the interaction between PVAc and CA. The intrinsic properties of CA alone, which increase the water-resisting capacity of PVAc, result in an insoluble polymer layer. Fig. 1d–f confirms the presence of Cu-NPs by high-resolution TEM (HR-TEM), in which the small particles can be identified as metallic Cu by the lattice fringes of Cu (111).[4,41] The fringes revealed by TEM reaffirmed the existence of metallic Cu, which infers that Cu^{2+} ions from $Cu(NO_3)_2$ successfully undergo a reduction reaction. In addition, it is interesting to note that PVAc plays an important role in protecting metallic Cu-NPs from oxidation in ambient air. Due to the presence of CA, the self-assembled polymer chains became more compact and easily interact with each other, resulting in the uniform growth of small and independent Cu-NPs within the polymer chains.

EDS mapping is indicated in Fig. 1g–i to ascertain the elemental composition of the layer. The EDS spectrum confirmed the presence of C and Cu, indicating PVAc and Cu-NPs, respectively, in Cu-PVAc@MgO. Owing to the high porosity, surface area and good ability to absorb the polymer, the MgO support promotes the embedment of the polymer and Cu-NPs. Plenty of reports in conventional synthesis methods have shown that incorporating more elements typically results in heterogeneous and segregated structures. This reduction-immobilizing method could overcome these drawbacks by generating an *in situ* reduction phenomenon of Cu precursors in polymers deposited onto MgO supports.

2.2. Compositional analysis of Cu-PVAc@MgO

To verify that Cu-NPs were successfully prepared by Cu-PVAc@MgO, the chemical constituents were analyzed by X-ray diffraction (XRD), as presented in Fig. 2a, with peaks predominantly assigned to metallic Mg, MgO and Mg_2SiO_4. The characteristic peaks of Mg (JCPDS no. 00-035-0821) are observed due to the extent of strong X-ray penetration. Diffraction peaks detected at $2\theta = 32.42^\circ$, 38.42°, 44.72°, and 81.92° were assigned to Mg_2SiO_4 (JCPDS no. 00-004-0768) as a result of the interaction between the Mg substrate and ions generated from the electrolyte during PE, while peaks at 36.82°, 43.07°, 63.37°, and 78.27° corresponded to MgO (JCPDS no. 01-078-0430). Likewise, the broad peak of the polymer in the Cu-PVAc@MgO sample when compared to that of the MgO sample was detected as an amorphous peak.[42] A recent report showed that crystalline Cu peaks were not detected by XRD since the concentration was low and the size of Cu-NPs was extremely small, in agreement with our experimental observations.[43,44] In addition, the relatively high intensity of MgO compared to Cu-NPs meant that the presence of Cu-NPs was unlikely to be detected.

Further Fourier transform infrared (FT-IR) spectra of both the Cu-PVAc@MgO and MgO samples were recorded, as depicted in Fig. 2b. The functional groups present in the polymer were indicated by several sharp and intense peaks. The predominant peak at 1729 cm^{-1} is assigned to the C=O stretching vibration associated with the ester network of acetate groups.[45] This peak was complemented by two less intense peaks at 1433 and 1370 cm^{-1} due to the $-CH_3$ asymmetric and symmetric bending vibrations, respectively. The second most intense peak was detected at 1225–1016 cm^{-1}, followed by a less intense peak at 947 cm^{-1}, showing the asymmetric C–O

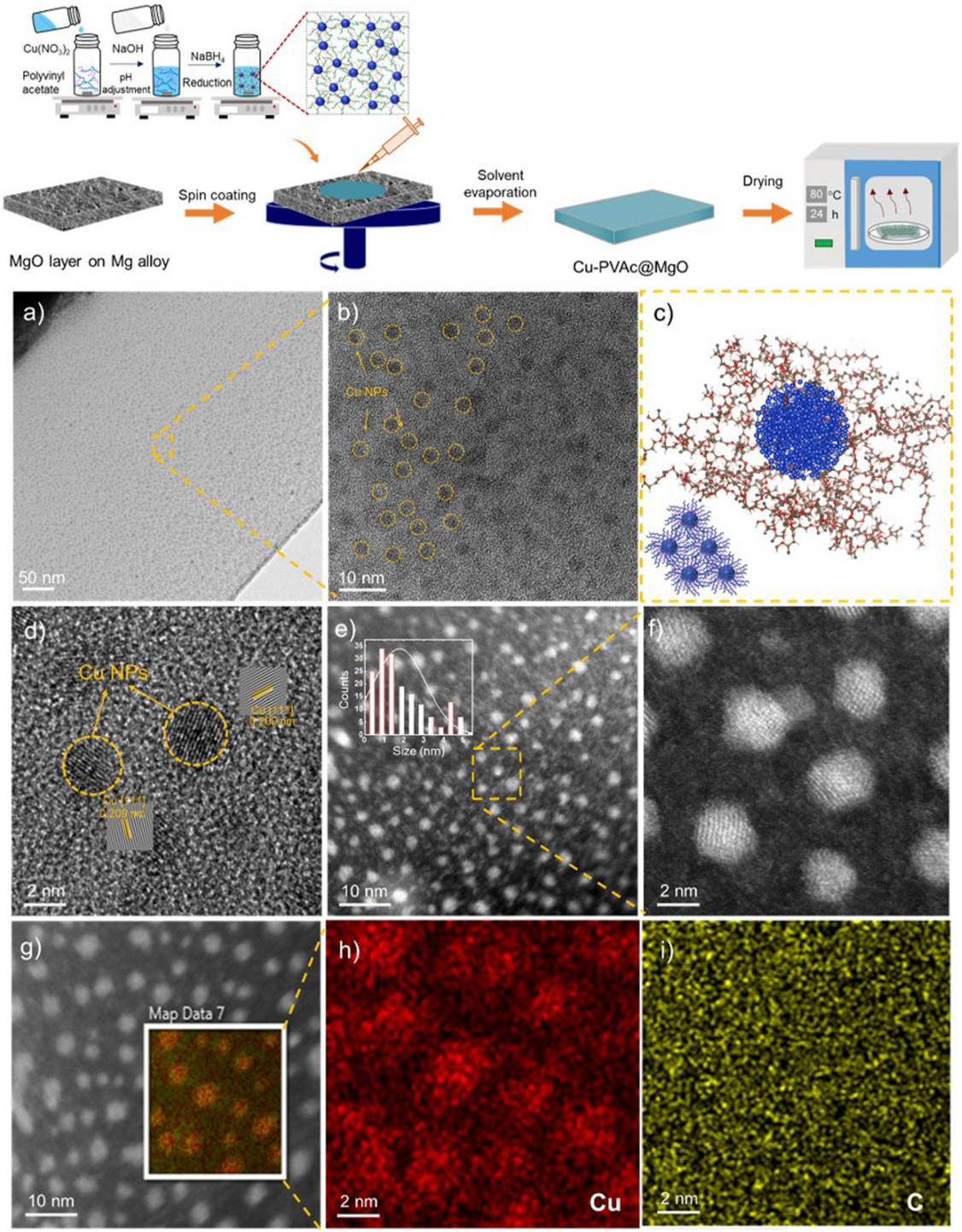

Fig. 1 Schematic illustration of the reduction-immobilization strategy in preparing the Cu-PVAc@MgO catalyst. Morphological characterization by (a) low magnification TEM, showing the uniform distribution and size of Cu NPs, and (b) TEM, showing the spherical shape of Cu-NPs as marked by circular dots. (c) Illustration of Cu-NPs surrounded by PVAc. (d) HR-TEM identifying the lattice distance of Cu-NPs. (e) HAADF-STEM image of Cu-PVAc @MgO with the size distribution, indicating that the size of one NP cluster is mostly between 1–2 nm. (f) HR-HAADF-STEM image of Cu-NPs, (g) HAADF-STEM image of Cu-NPs and the corresponding mapping area of (h) copper and (i) carbon.

stretching mode of ester groups. Furthermore, doublet peaks of $-CH_3$ and $-CH_2$ asymmetric stretching vibrations at 2973–2926 cm^{-1} were detected. The peaks of the functional groups in the as-prepared PVAc are in agreement with the initial PVAc, as depicted in Fig. S5 (ESI†), confirming the successful deposition of PVAc onto MgO. Meanwhile, the peak at 3463 cm^{-1} was assigned to –OH as a result of the crosslinking behavior of PVAc with CA. Meanwhile, in the MgO sample, the characteristics of

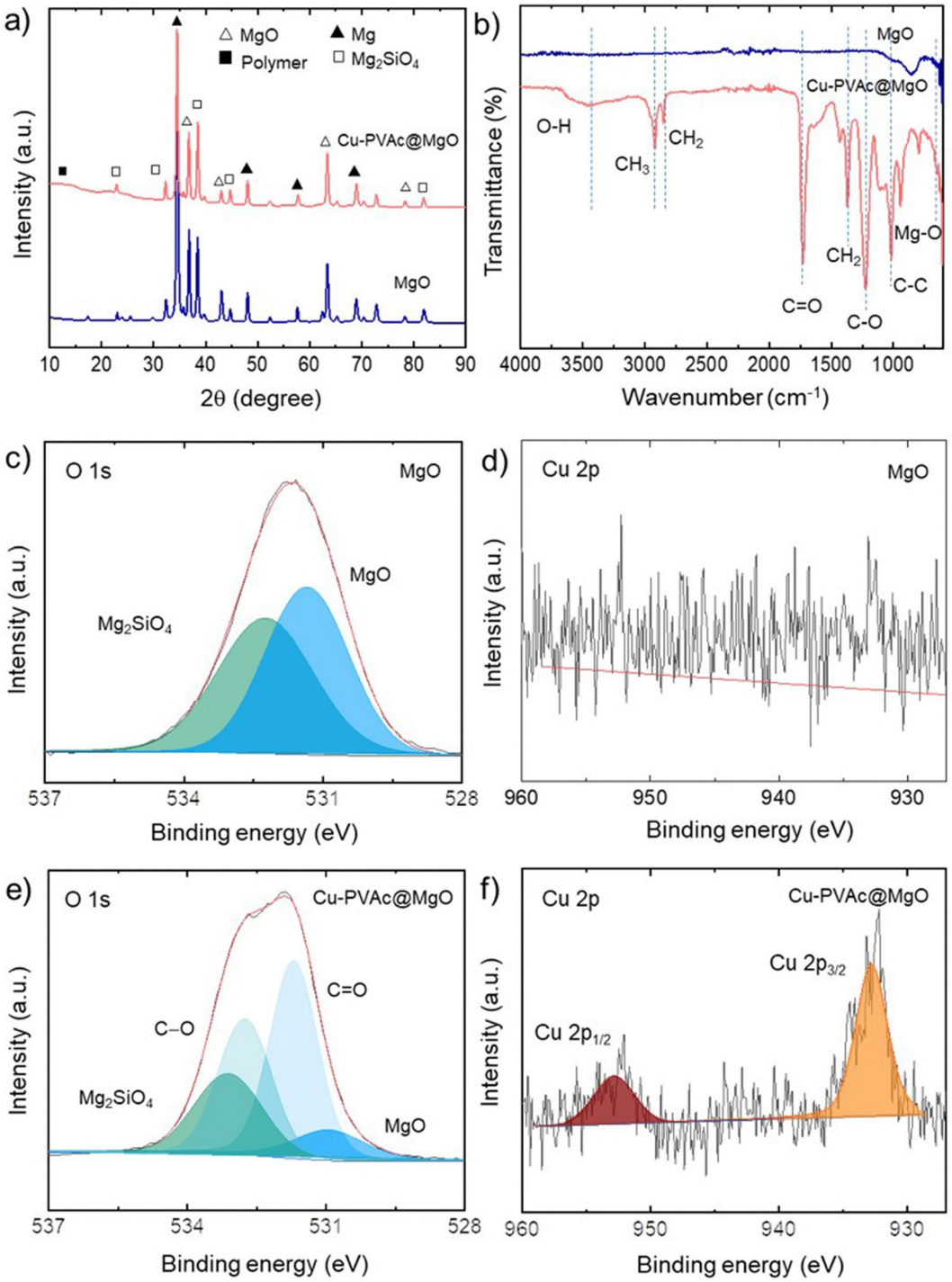

Fig. 2 Chemical composition of Cu-PVAc@MgO showing (a) X-ray diffraction spectra and the corresponding peaks, (b) Fourier transform infrared spectra with the associated functional groups as highlighted by dotted lines. Deconvolution XPS spectra at the core level of (c) O 1s and (d) Cu 2p of MgO. The peak of Cu 2p was not presented due to the absence of Cu NPs. Deconvolution XPS spectra at the core level of (e) O 1s and (f) Cu 2p of Cu-PVAc@MgO. Additional peaks were clearly seen in O 1s and Cu 2p as a result of Cu-PVAc deposition on MgO.

the bands related to Mg–O stretching modes were noted at approximately 700 cm^{-1}, and similar peaks with lower intensity were detected in the Cu-PVAc@MgO sample.

The surface chemistry of the synthesized polymer-embedded Cu-NPs was further determined by X-ray photoelectron spectroscopy (XPS) to investigate the oxidation states of the elements. The XPS survey spectrum in Fig. S6a (ESI†) clearly depicts the existence of Mg 1 s, O 1 s, and Si 2p. Although it is difficult to observe the Cu 2p peak in the XPS survey spectrum due to the low concentration of Cu-NPs, the deconvolution of

Cu 2p was accordingly fitted to present the peak. The high-resolution (HR)-XPS profile corresponding to Mg 1 s in Fig. S6b and c (ESI†) refers to the presence of MgO and Mg_2SiO_4 at 1303.28 and 1304.28 eV in both the MgO sample. Other peaks found at binding energies of 531.38 and 532.28 eV in O 1 s (Fig. 2c) shows the interaction originating from MgO and Mg_2SiO_4. It is apparent from the XPS peak that the MgO sample displays no binding energy peak of Cu (Fig. 2d). Meanwhile, the additional two peaks shown in Fig. 2e at 531.68 and 532.78 in the O 1 s orbital were ascribed to C═O and C–O, respectively, from Cu-PVAc@MgO. The presence of Cu-NPs is indicated in the HR-XPS spectra of Cu 2p at 932.38 and 952.68 eV, showing the energy splitting of Cu $2p_{3/2}$ and Cu $2p_{1/2}$, respectively (Fig. 2f). The existence of Cu^0 is confirmed by the peak in the Cu 2p XPS profile of the Cu-PVAc@MgO catalyst. Despite the low concentration of Cu, its presence is suggested to be stable; otherwise, weak satellite features would be recorded between the Cu $2p_{3/2}$ and Cu $2p_{1/2}$ binding energies.[46] The compositional analyses of Cu-PVAc@MgO through XPS were in line with the XRD and FTIR results, suggesting that Cu-NPs were successfully embedded by PVAc molecules.

Another upmost prominent factor in determining polymer stability is the measurement of thermal stability. The thermal properties of the polymers were investigated by TGA, as displayed in Fig. S7 (ESI†). The removal of adsorbed volatiles was followed by the elimination of water molecules on the sample surface due to high temperature, resulting in a mass loss of 17.55% in the temperature range of 150 °C up to 240 °C, followed by 50.41% mass loss, indicating the elimination of acetic acid, which is continuously removed until approximately 390 °C.[47] In the case of Cu-PVAc@MgO, this gradual mass loss could be attributed to the elimination of physically absorbed volatiles followed by the subsequent decomposition of acetic acid.

In the case of the control sample (PVAc), the main decomposition stage begins at 300 °C, resulting in a drastic mass loss of up to 62% when the curves almost overlap at approximately 360 °C, indicating a decomposition process ascribed to the dehydroxylation reaction and the release of acetic acid due to PVAc degradation. After the temperature reached 390 °C, a similar decomposition process can be observed for both Cu-PVAc@MgO and PVAc. Consequently, the thermal analysis accurately detects the similarities between the synthesized polymer film (Cu-PVAc@MgO) and the standard film (PVAc). Taking into consideration the aforementioned factors, Cu-PVAc@MgO may emerge as a potential catalyst material that remains stable even for a reaction taking place at high temperature without any decomposition risk up to 250 °C.

2.3. DFT and PDOS study of Cu-PVAc@MgO

To elucidate the electronic contribution of the Cu-PVAc@MgO system, the interaction between each system was elaborated at the molecular level by density functional theory (DFT) and the density of states (DOS). The calculations were derived following the optimization of the adsorption energy in each system consisting of polymer, Cu-NPs, and MgO, showing that the Fermi level was set to zero, as indicated by the dashed line. Fig. S8 (ESI†) shows the partial DOS (PDOS) of Cu NPs and PVAc, which demonstrate the distinctive relative height of the curves at different energy regions, implying that among the two systems, Cu-NPs have a higher contribution to the molecular orbitals than PVAc.

An optimized structure consisting of Cu-NPs, PVAc chains, and MgO is illustrated in Fig. S8 (ESI†) along with the presence of hydrogen bonding. PVAc provided a number of hydrogen bonds through CH_3COO^- to interact with the MgO layer, which is attributed to the hydrogen atom in the polymer and the oxygen atom in MgO. This bond is suggested to be responsible for the intermolecular force that promotes the adhesion strength of PVAc to the interface of MgO. Meanwhile, the bonding strength between PVAc and Cu-NPs would be associated with the interaction among Cu atoms with carbon and oxygen from PVAc, as depicted in Fig. S8 (ESI†). The atomic distance of Cu with carbon was calculated to vary at 1.43, 1.50, 1.55, 1.72, and 1.92 Å, which shows a strong interaction between Cu and carbon atoms originating from the polymer. On the other hand, the interatomic distances between Cu and oxygen of the polymer chains are 1.52, 1.75, 1.68, and 1.77 Å, suggesting additional strong interactions, as further verified by the interaction between Cu and PVAc shown in Video S1 (ESI†). These results suggest that Cu is strongly embedded in the polymer with a low possibility of leaching out of the catalyst system, which further leads to the high stability of Cu-PVAc@MgO.

2.4. Catalytic performance of Cu-PVAc@MgO supported by DFT calculations

The reduction of nitroarene compounds such as 4-nitrophenol (4-NP), 1,3-dinitrobenzene, 1-bromo-2-nitrobenzene, 1,4-dinitrobenzene, 4-nitrotoluene, and 1,2-dinitrobenzene to the corresponding amines was evaluated using sodium borohydride ($NaBH_4$) as a hydrogen donor. The reduction reaction is unlikely to proceed without the addition of catalyst, as the absorption profile remains nearly constant, as seen in Fig. 3a, after keeping the reaction mixture for 2 h due to the lack of electron transfer from BH_4^- to 4-NP. In contrast, the reduction of 0.036 mM 4-NP using a 6.25 cm^2 area of Cu-PVAc@MgO with 0.165 M of hydrogen donor started to produce 4-aminophenol (4-AP), which subsequently reaches nearly 100% conversion, as depicted in Fig. 3b. Upon the addition of the catalyst, the absorbance peak corresponding to 4-NP at ~400 nm rapidly declined along with the reaction time, demonstrating a robust catalytic reduction, in which almost all 4-NP had been converted to 4-AP. In the meantime, completion of the reaction was confirmed by a change in color in the reaction solution from yellow to colorless as well as a simultaneously formed new absorbance peak at 285 nm monitored by UV-Vis absorbance at regular intervals, which belongs to 4-AP.

To further evaluate the performance of the Cu-PVAc@MgO catalyst, a reduction of 4-NP was carried out over MgO in the presence of a hydrogen donor, which showed no noticeable reduction peak in the range of 250–500 nm (Fig. S9a, ESI†); this

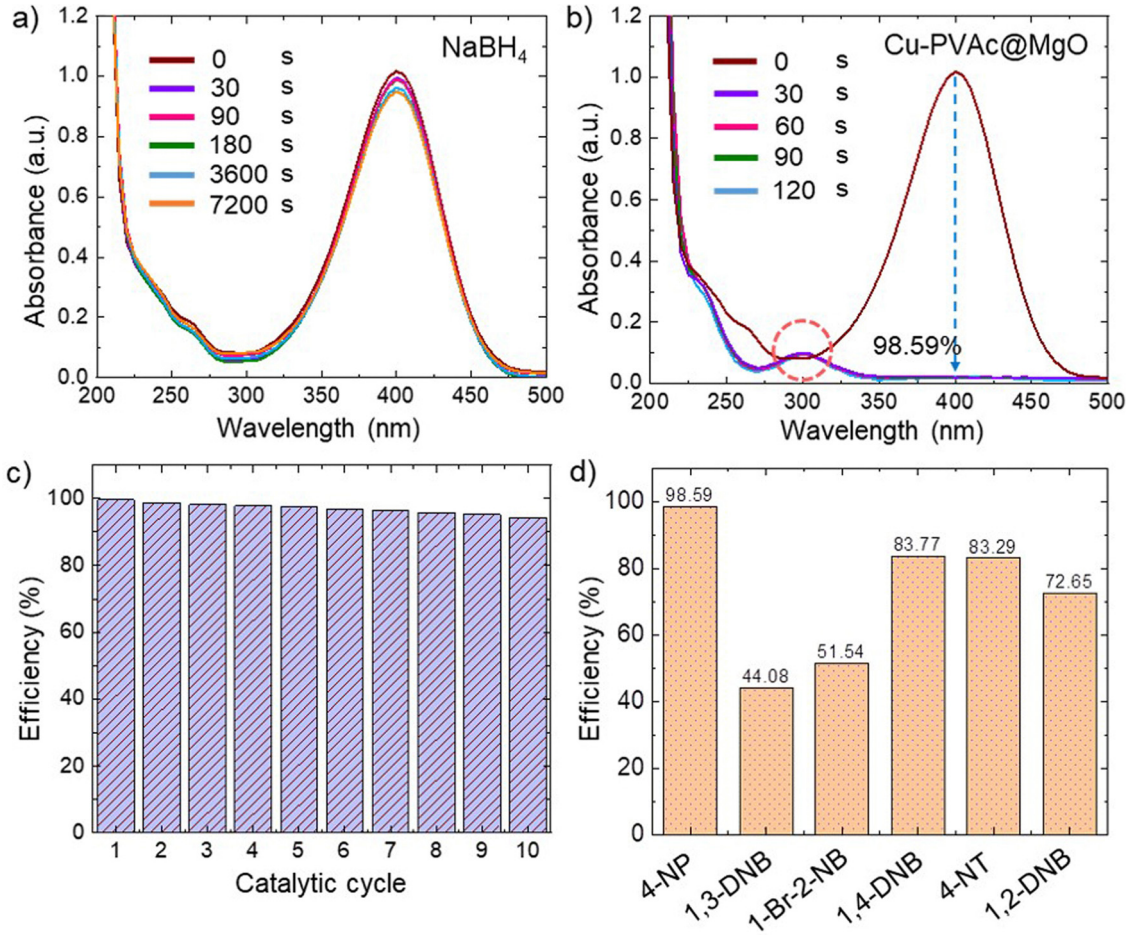

Fig. 3 Time dependent UV-Vis spectra during the catalytic reduction upon 5 ppm 4-NP (a) without the presence of Cu-PVAc@MgO and (b) over Cu-PVAc@MgO. (c) The durability of the Cu-PVAc@MgO catalyst after 15 consecutive cycles showing that the efficiency declined insignificantly. (d) Efficiency of Cu-PVAc@MgO with varying nitro compounds.

indicates that MgO shows no catalytic activity.[48] The reusability of the Cu-PVAc@MgO catalyst was investigated for 15 cycles of consecutive reactions under the same conditions. The results indicated that the catalyst could reach at least 15 cycles with an insignificant decline in the catalytic activity even after the 15 cycles, suggesting excellent catalytic stability, as depicted in Fig. 3c. Furthermore, there was no need to increase the reaction temperature, time or pressure, which are often prerequisites to carry out a reaction. The reduction of a wide variety of compounds was evaluated accordingly (Fig. 3d), showing that the catalyst might undergo diverse reduction reactions. However, the catalytic system was found to be efficient regardless of the presence of electron-withdrawing or electron-donating groups. Interestingly, the catalytic performance of Cu-PVAc@MgO in 4-NP presented the highest percentage among the reported compounds, with detailed absorbance curves of each sample shown in Fig. S9b–f (ESI†). To ensure that the catalytic reaction occurred efficiently without the limitation of the polymer layer, a UV-Vis absorbance profile is provided in Fig. S10 (ESI†) upon a sample containing a MgO-polymer layer without the existence of Cu NPs. This suggested that Cu NPs are indeed the active site of the catalyst system.

The reduction of nitroarenes with *para*-geometries having electron-donating groups generated higher product yields than those of *ortho* and *meta* geometries; this is due to the steric hindrance arising from the spatial arrangement of the functional groups in nitroarene compounds,[49,50] which is in line with the adsorption energy of 4-NP. Upon increasing the Cu content of Cu-PVAc@MgO, the same experimental conditions were assessed in different amounts of PVAc and Cu NPs to determine the efficiency of each composition according to the performance, as shown in Fig. S11a and b (ESI†). The greatest performance was achieved when the concentrations of Cu-NPs and PVAc were 1 g L^{-1} and 1.5 g L^{-1}, respectively.

The analysis of XRD and FT-IR before and after the reduction reaction (similar peaks are shown in Fig. S12a and b (ESI†) of Cu-PVAc@MgO) confirmed the sustainability of the structural integrity and robust stability of the Cu-NPs. In addition to the FT-IR and XRD analysis of Cu-PVAc@MgO after 15 consecutive cycles of reduction, the SEM and TEM shown in Fig. S13a and b (ESI†) indicated no change in the Cu-PVAc surface which also confirmed the strong Cu–polymer interactions. Considering the preparation strategy, direct deposition of Cu-NPs by a wet chemical method without embedment in a

polymer matrix onto the MgO surface showed a considerably lower efficiency and a drastic decline in catalytic performance over 5 cycles (Fig. S14a and b, ESI†). This result was achieved due to the irregular distribution and detachment of Cu-NPs from the catalyst. It is worth noting that the catalysts fabricated using our method possess exceptional resistance to aggregation as well as the stability of the supported Cu-NPs, which leads to not only a uniform distribution of NPs but also rapid catalytic performance. Thus, it might be concluded that the polymer assisted the binding of Cu-NPs on the MgO support, preventing the loss of NPs, which is responsible for the catalytic activity.

The kinetic parameter value, which is the reaction rate, was determined to determine the activation energy for reduction to occur. The pseudo-first-order kinetics presented in eqn (1) are suitable to calculate the reaction rate since the concentration of 4-NP is much lower than that in $NaBH_4$.

$$\ln\frac{A_t}{A_0} = \ln\frac{C_t}{C_0} = -k_{app}t \quad (1)$$

where A_t and A_0 represent the absorbance of the initial 4-NP and residual 4-NP at 400 nm after reduction, respectively; C_t and C_0 are the concentrations of 4-NP corresponding to A_t and A_0, respectively; and k_{app} is the apparent rate constant. Linear growth could be used to fit the correlation between $\ln(C_t/C_0)$ and reaction time t, while each k_{app} value can be measured from the slope, as shown in Fig. S15 (ESI†), which displays the results of 4-NP reduction reactions catalyzed by Cu-PVAc@MgO at different reaction temperatures, demonstrating that a temperature rise has a positive effect on the reaction kinetics. As shown in Fig. S15 (ESI†), the k_{app} value increases from 0.0319 to 0.0374 s^{-1} as the reaction temperature increases from 25 to 45 °C. The k_{app} value indicated a reaction rate in reducing 4-NP, to which a comparison with the reported noble metal and Cu-based catalysts is shown in Table S1 (ESI†), implying that the reaction rate of the current catalyst material is the highest among the reported catalyst systems. By determining the value of k_{app}, according to the Arrhenius equation, the activation energy (E_a) of a reaction can be determined by the following equation:[51]

$$\ln k_{app} = \ln A - \frac{E_a}{RT} \quad (2)$$

where A denotes the Arrhenius factor; R is the universal gas constant (8.314 J (mol K)$^{-1}$), and T is the corresponding temperature of the reaction. The value of the activation energy (E_a) is calculated to be 8.36 kJ mol^{-1} according to the linear plot of $\ln k_{app}$ against $1/T$, which is significantly lower than the recent reports for metal-based catalysts, such as Cu_xO/Cu/NC (50.7 kJ mol^{-1}),[52] Pd/SiO_2-p-NIPAM (37 kJ mol^{-1}),[53] $Cu_{60}Ni_{40}$–CeO_2 (39.6 kJ mol^{-1}),[54] Au/PMMA (38 kJ mol^{-1}),[55] and PtCoY (55 kJ mol^{-1}).[56] These results reveal that even without elevated temperature (*e.g.*, ambient temperature), Cu-PVAc@MgO is at least comparable or even superior to that of several reported cases[54,55,57,58] in driving the 4-NP reduction, and thus, Cu-PVAc@MgO emerges as a potential catalyst; this is because three factors are responsible for this high and robust catalytic activity: (1) the small size and high dispersion of Cu NPs on the support surface *via* the reduction-immobilization strategy, (2) the as-prepared Cu-PVAc@MgO catalyst does not require an induction period, and (3) the borders and perimeter beside the embedded structure of Cu NPs with PVAc on the MgO surface can generate abundant active sites that are critical for achieving high catalytic performance.

The reduction reaction of 4-NP to 4-AP was further monitored by *in situ* Raman absorbance (Fig. S16, ESI†), showing the characteristic of functional groups attributed to the reduction of 4-NP producing 4-AP. According to the spectra, three stable peaks at ~576, ~1098, and ~1657 cm^{-1} were ascribed to the C–H asymmetric stretch of the aromatic ring, while two new peaks at ~862 and ~1299 cm^{-1} were associated with N–H asymmetry and symmetry, respectively.[59] These vibration signals indicated that NO_2 was successfully reduced to NH_2 within 30 s in the presence of the catalyst. Further analysis of the final product was conducted through LC-MS, as depicted in Fig. S17 (ESI†), revealing that the mass spectrometer indicated an m/z value of 110.06, which aligns with the mass-to-charge ratio of 4-AP.

In comparison to the conventional powder catalysts, which are difficult to directly employ in dynamic catalytic reactions, Cu-PVAc@MgO shows advantages. In some cases of powder catalyst, weak active particle–support interactions yield highly catalytic activity but difficult to avoid detachment and leaching from the support surface during the reduction reaction. Thus, numerous efforts have been made in an attempt to avoid metal leaching by enhancing the interaction between metal NPs and the support.[60–62] However, in this catalyst system, the detachment of catalyst active sites into the solution could be prevented since the polymer binds the nanoparticles firmly to the support. In addition, embedding Cu-NPs in PVAc would retain itself from natural agglomeration and inevitable oxidation during the catalytic reaction. Thus, the combination of MgO and Cu-NPs proved to show a synergistic action in reducing nitro groups into amines since electron transfer improves the catalytic performance.[63,64] Moreover, not only the electron transfer, but also the adsorption of organic molecules (4-NP) influences the catalytic activity. It is suggested that this reaction is highly influenced by the MgO support since it provides a high adsorption capacity.[65,66] This reveals the effects brought by the adsorption of 4-NP at the surface of the catalyst material and electron transfer behavior of Cu active sites that are responsible for catalytic performance, overcoming the long-standing challenge of catalyst materials by providing both functionality and stabilization.

To further identify the catalytic performance, the mechanism pathway proposed in this work is illustrated in Fig. 4a: BH_4^- and 4-nitrophenol were sequentially adsorbed on the Cu-NP surface with the assistance of MgO. The adsorption of 4-NP molecules at the surface of the catalyst prior to reduction is mainly due to electron transfer between Cu-NPs and BH_4^-, which leads to the hydrogenation reaction of nitro groups. Due to the high ability of Cu^0 to transfer electrons, it facilitates the electron transfer of BH_4^-, as it is highly active and responsible

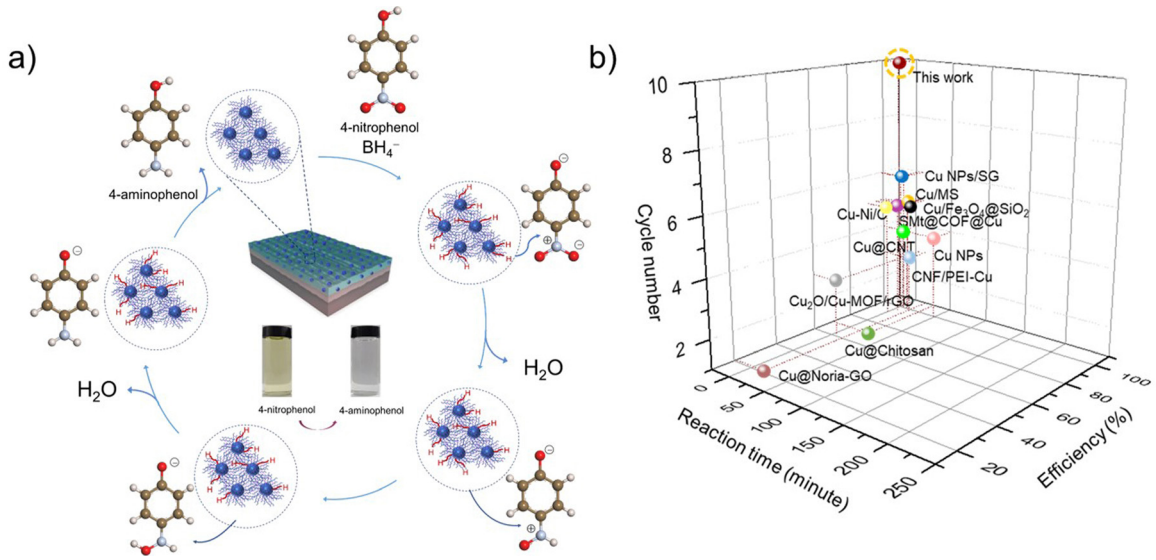

Fig. 4 (a) Reduction mechanism of 4-NP to 4-AP over Cu-PVAc@MgO involving adsorbed hydride at the surface of the catalyst. (b) The catalytic efficiency, reaction time, and stability of Cu-PVAc@MgO in comparison with the reported Cu-based catalysts.

for the hydride transfer reaction.[26,67] In addition, the basic nature of MgO and the acidic properties of 4-NP result in acid-base interactions. The basic sites of MgO, which are primarily associated with the presence of oxygen ions on the surface, have the ability to accept protons from the hydroxyl group in 4-NP, giving rise to the affinity toward 4-NP, allowing for adsorption to occur easily.[68,69] Therefore, the basic nature of the MgO support plays a prominent role in assisting the adsorption step, which is in line with the absorbance curve drawn in Fig. 3a.

The catalytic steps are then followed by surface-hydrogen species indicated by the formation of hydrogen bubbles at the catalyst interface and electron transfer from BH_4^- to 4-NP to produce 4-AP prior to the desorption process of 4-AP. $NaBH_4$ was adsorbed and desorbed on the surface of Cu-NPs, and copper hydride was formed due to the dissociation of H from $NaBH_4$. Subsequently, hydrogen and electrons transferred to the nitro group of 4-NP, which was converted into 4-AP after hydrogenation along with the color change of the solution from yellow to colorless. 4-AP was then desorbed from Cu-NPs and took part in the catalytic reaction again. This suggests that the outstanding catalytic performance during the reduction of 4-NP can be attributed to the synergistic behavior between the MgO support and polymer-embedded Cu-NPs.

The presence of Cu-NPs embedded in the polymer matrix would result in a hydrogen atom (H) from $NaBH_4$ to form a bond with Cu, known as Cu-hydride, which leads to the promotion of electron transfer from BH_4^- to 4-NP, resulting in the initiation of the hydrogenation process. To further elucidate the catalytic activity of Cu-PVAc@MgO, a synergistic catalytic mechanism between the three systems was proposed. The mechanism suggests that an efficient adsorption of reactants and rapid hydrogen transfer from BH_4^- to 4-NP over Cu-PVAc@MgO governs the reduction of 4-NP. The electron transfer caused Cu NPs to be electron-deficient and become electrophilic. In the presence of BH_4^-, due to the weak basicity of $NaBH_4$, the molecules deprotonate and trigger the formation of 4-nitrophenolate ions. Subsequent to the adsorption process promoted by MgO, the negatively charged 4-nitrophenolate and BH_4^- ions preferentially react with the electrophilic Cu-NPs. Meanwhile, the BH_4^- ions donate electrons to the electron-deficient Cu-NPs and generate active hydrogen atoms that are suggested to be responsible for the hydrogenation of 4-NP.[70] Due to thermodynamically unstable hydrogen atoms, it readily reacts with 4-nitrophenolate ions, releasing bubbles as evidence of their presence since the unreacted hydrogen species might bind with each other and generate H_2 gas.[71] This process continued for at least 15 cycles, which was attributed to the uniform size and distribution of Cu-NPs grafted throughout the polymer layer.

The efficient catalytic performance based on three crucial parameters, including reaction time, efficiency, and recyclability, of this catalyst material was compared with other Cu-based catalysts, and it is worth noting that the catalyst in our work outperforms the reported cases,[72–81] as described in Fig. 4b. This result highlights the prominent strategy between Cu-NPs and the polymer matrix, which effectively brings the underlying mechanism in enhancing the catalytic reaction of 4-NP.

To shed some light on the reduction reaction and mechanism in the presence of a catalyst that exhibits high catalytic performance, a computational study by DFT simulating the physical adsorption energy (ΔE_{ads}) during the reduction of 4-NP by Cu-PVAc@MgO was performed to elucidate the interactions between four systems consisting of 4-NP, polymer, Cu-NPs, and MgO in a four-cell system. Several geometries of 4-NP were drawn based on the optimization of its position. These positions showed that 4-NP could undergo several geometries during reduction reactions. Some molecules were adsorbed in the parallel geometries to the metal surface *via* an aromatic

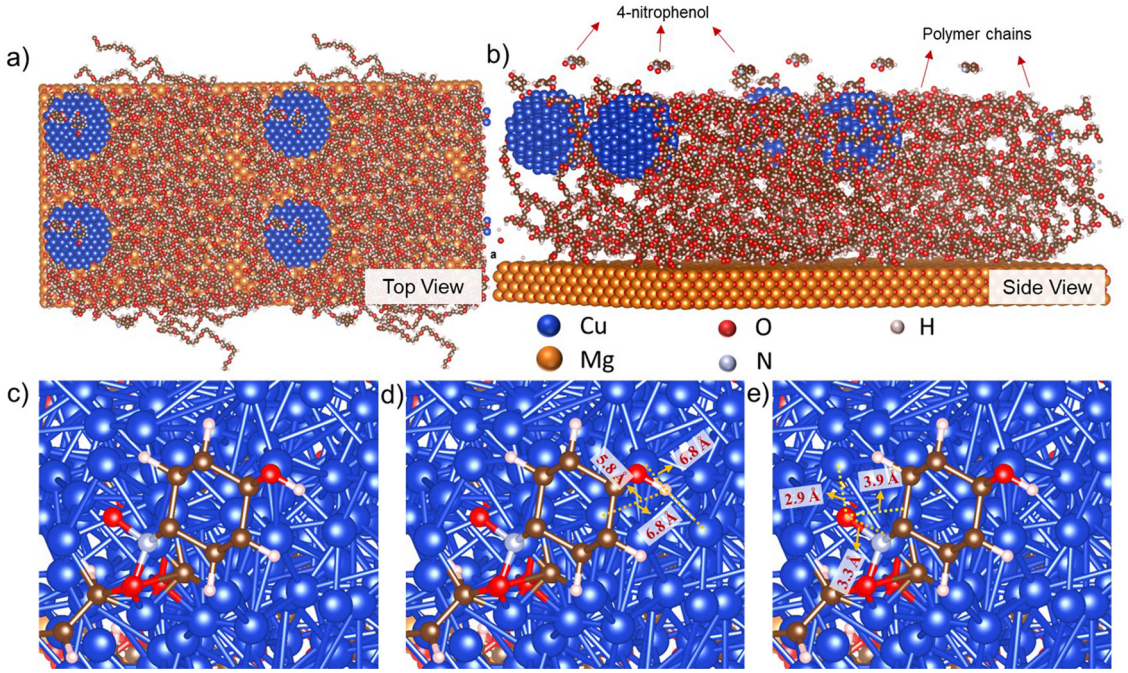

Fig. 5 Catalytic mechanism supported by computational simulation in regards with the catalytic behavior of 4-NP molecules with Cu-PVAc@MgO taken from the optimized (a) top view and (b) side view. (c) Bonding interaction of Cu-PVAc@MgO and the 4-nitrophenol compound with the closest interacting atoms between Cu NPs and 4-nitrophenol *via* (d) –OH and (e) $-NH_2$ functional groups.

ring, which is facilitated by the interaction between the phi electron of 4-NP and the surface of MgO. Different geometric configurations perpendicular to each other were also employed to further understand the optimum adsorption reaction.

The adsorption energy of 4-NP on the surface of the catalyst was determined to understand the interactions between reducible $-NO_2$ functional groups and Cu-PVAc@MgO. Fig. 5a–e depicts 5 molecules of 4-NP with different adsorption geometries to illustrate the preferred position during the catalytic reaction, as we may understand that during the catalytic reaction, it can generate two common geometries: parallel and perpendicular. However, under concrete conditions, some molecules may not bind to the catalyst in parallel and perpendicular directions. As a result, the adsorption energy produced by these geometries ranged from -97 kJ mol^{-1} to -125.23 kJ mol^{-1}, with an average value of -111.12 kJ mol^{-1}. According to the calculation, most of the geometries were either parallel, perpendicular, or tilt to some degree, showing that $-NO_2$ groups facilitated the reaction of 4-NP molecules to the catalyst. As depicted by the adsorption results, $-NO_2$ groups were directly facing the catalyst surface on the side of the Cu-NPs due to the electron-deficient Cu-NPs being drawn by electron-rich $-NO_2$, which is in line with previous studies.[82] The atomic distance between $-NO_2$ and the closest Cu atom is revealed to be less than 3 Å (2.90 and 2.93 Å), which is far shorter than that of –OH sites with the closest Cu atom (5.70 and 5.80 Å), indicating that adsorption *via* $-NO_2$ groups is stronger than that of –OH groups, according to Fig. 5b–d. Thus, the preferable adsorption site of 4-NP to the catalyst surface is *via* $-NO_2$ bonding, which is readily converted into $-NH_2$, leading to a successful and efficient reduction reaction of 4-NP. Finally, the bonding between 4-NP and Cu-PVAc@MgO is essential for establishing the relationship between structure and performance, enabling the development of advanced catalyst materials. The microstructural and compositional analyses confirm the successful fabrication of a distinctive structure offering active sites resulting from uniformity in the size and distribution of NPs. Moreover, in the case of polymer layer deposition, several previous studies reported the wavy surface due to the naturally formed roughness features of the MgO layer as a result of high temperature plasma through the PE method, whilst the Cu-PVAc layer was grown on MgO by spin coating to reduce the non-uniformity of the Cu-PVAc layer, as shown in Fig. 1a. This finding offers a remarkable enhancement in facilitating efficient catalytic reactions.

In most recent studies, a polymer was used as a stabilizing agent during the synthesis of Cu-NPs *via* a conventional wet method so that the products would remain stable against oxidation. Nevertheless, this method still induces aggregation due to Cu-NPs having a high surface area. Thus, our work provides direct visualization of the *in situ* reduction of Cu^{2+} to Cu^0 inside the polymer matrix on magnesium oxide supports and clarifies the details of the suppression and uniform distribution of Cu NPs during the mixing of Cu-NPs into the PVAc polymer matrix on the porous support surface. In the case of the current investigation, the formed mixture consisted of Cu-NPs dispersed in the PVAc matrix, which were relatively stable in air, unlike the generally susceptible Cu-NPs to oxidation. To avoid the aggregation of the Cu NPs in the polymer network, the pH was kept at neutral to almost alkaline because pH $>$ 7 facilitates the dispersion of the polymer by deprotonation of the carboxylic group becoming carboxylate ions. Subsequently,

the negatively charged carboxylate ions facilitate the incorporation of positively charged copper ions into the polymeric network. The role of PVAc in generating Cu-PVAc@MgO is summarized in two aspects: (i) PVAc can adsorb onto the surface of Cu NPs, forming Cu-PVAc and thus inhibiting the oxidation of Cu NPs by water and oxygen; (ii) PVAc can act as a size regulator by limiting the mobility of Cu NPs and preventing the growth of NPs due to the dense polymer. Moreover, the polymer chains were held by a crosslinking agent, so the bonding between the chains was stronger than that without a crosslinking agent. Importantly, R-IS treatment provides intermolecular repulsion forces as a steric stabilization due to the large molecules, as in polymer chains surrounding a Cu NP surface, establishing a protective layer and suppressing aggregation. If the interparticle distance of large molecules (polymer) was decreased, the aggregation of Cu NPs would be hindered due to an increase in the density of molecules adsorbed in the interparticle space. Notably, this would cause a decline in entropy, giving rise to Gibbs free energy, which is thermodynamically not favorable. Thus, the increased density is responsible for the growth of repulsive forces. In addition, a higher volume ratio of PVAc compared to the metal precursor leads to a decrease in the interparticle space of the adsorbed molecules.[83] As a result, the particle movement would be limited by the density of PVAc, resulting in a uniform distribution and uniform size of NPs. These results clarify the formation of Cu-PVAc on the surface of the MgO support, which completely differs from conventional methods with ligand adsorption or stabilizing agents to produce NPs, as it only provides reproducibility and relatively long-term stability.

3. Conclusions

In summary, Cu-PVAc@MgO was successfully fabricated *via* a reduction-immobilizing strategy, in which Cu precursors were reduced by exposure to sodium borohydride, yielding Cu-NPs within the polymer, overcoming the limitations of the catalyst system. These composite thin films exhibited robust catalytic properties closely associated with ultrasmall NPs. Cu-NPs are responsible for the high catalytic activity owing to their uniform size and distribution, which efficiently promotes electron transfer between the reducing agent ($NaBH_4$) and organic compounds by the formation of Cu-hydride. Polymers provide a stable environment, as they hinder Cu-NPs from being oxidized. As a result, high efficiency and stability of the catalyst materials were possibly achieved by up to ten cycles. These discoveries provide great alternatives for state-of-the-art catalyst design, especially in the field of environmental remediation.

4. Methods

4.1. Reagents and materials

Copper nitrate $Cu(NO_3)_2{\cdot}3H_2O$, polyvinyl acetate beads with average MW ~10 000 by GPC, citric acid, ethyl alcohol anhydrous, sodium hydroxide (NaOH), potassium hydroxide (KOH), sodium silicate (Na_2SiO_3), sodium borohydride ($NaBH_4$), 4-nitrophenol (4-NP), 1,2-dinitrobenzene (1,2-DNB), 1,3-dinitrobenzene (1,3-DNB), 1-bromo-2-nitrobenzene, and 4-nitrotoluene used in this experiment were of high purity grade obtained from Sigma Aldrich. All chemicals are used as received without further purification. Pure water was obtained from a Milli-Q water purifier.

4.2. Fabrication of the MgO support

The initial substrate for the catalyst support used in the present study was an AZ31 Mg alloy sheet consisting of 2.89 Al, 0.96 Zn, 0.31 Mn, 0.15 Fe, 0.12 Si, and balance Mg (in wt%). The sample having dimensions of 30 mm (L) × 30 mm (W) × 4 mm (T) worked as an anode and a stainless-steel wire was employed as a cathode. Prior to plasma electrolysis (PE), the sample was polished mechanically using SiC paper up to #1200 grit, degreased with ethanol and dried in warm air. Subsequent PE treatments were carried out in an aqueous electrolyte containing KOH and Na_2SiO_3 at a concentration of 6 g L^{-1} and 8 g L^{-1}, respectively. The PE treatment was conducted for 300 s under an alternating current condition with a current density of 100 mA cm^{-2} and frequency of 60 Hz.

4.3. Synthesis of the Cu-PVAc@MgO catalyst

To synthesize a polymer suspension, the optimum ratio of polyvinyl acetate (PVAc) as a polymer and citric acid (CA) as the cross-linking agent was determined. An amount of 1.5 g PVAc was dissolved in 25 mL ethanol solvent prior to the addition of 1 g CA. The reaction was facilitated by heating and stirring at 60 °C for 2 h after which a transparent suspension was obtained. Afterward, 1 g $Cu(NO_3)_2{\cdot}3H_2O$ was dissolved in 10 mL ethanol, and subsequently 2 mL of the Cu solution was added dropwise to the PVAc suspension, and then the reaction was kept heated at the same temperature under stirring for 30 minutes. The pH of the solution was adjusted using NaOH up to 7–8 and then the reduction of Cu^{2+} to Cu^0 was done by using 0.25 mol L^{-1} $NaBH_4$ solution until the color changed into dark brown. Prior to Cu-PVAc layer deposition, the MgO layer was cleaned using ethanol. Subsequently, 1 mL of Cu-PVAc suspension was deposited on the MgO layer *via* spin-coating at 1000 rpm for 10 s followed by 3000 rpm for 20 s. The sample was cured at 60 °C in a closed system for 24 h to enhance the cross-linking bonds between PVAc and CA. After air-cooling, the resulting Cu-PVAc@MgO was used as a catalyst in aqueous conditions. A similar method was utilized to fabricate a different ratio of Cu precursor and polymer. Additionally, as a comparison to the current fabrication method, direct deposition of Cu NPs through a wet method was carried out without the presence of polymer. 1 g $Cu(NO_3)_2{\cdot}3H_2O$ was dissolved in 10 mL ethanol then directly deposited on the MgO layer *via* spin-coating at 1000 rpm for 10 s followed by 3000 rpm for 20 s. The sample was cured at 80 °C in a closed system for 24 h and used as a comparative sample to elaborate the catalytic activity of the Cu-PVAc@MgO catalyst.

4.4. Characterization of Cu-PVAc@MgO

The morphologies of the polymer nanoparticles formed by PE were observed using a scanning electron microscope (SEM, HITACHI, S-4800) equipped with energy-dispersive X-ray spectroscopy (EDS, HORIBA EMAX) for elemental analysis. The image analyzer was used to measure the average size of the nanoparticles. Constituent compounds were analyzed by X-ray diffraction pattern (XRD, RIGAKU, D-MAX 2500) with a step size of 0.05° within the scan range of 20–90°. The chemical composition of the composite coating was evaluated in detail *via* X-ray photoelectron spectroscopy (XPS, VG Microtech, ESCA 2000), Fourier transform infrared spectroscopy (FTIR, PerkinElmer Spectrum100), and Raman spectroscopy (Horiba, Explora Plus). The sample production prior to TEM observation was carried out by a Focused Ion Beam System (FIB, ZEISS AURIGA). Field-emission transmission electron microscopy (FE-TEM, Jeol JEM-ARM200F) was utilized to obtain high resolution images of the composite coating. The electron-transparent sample for TEM observation was prepared using focused ion beam (FIB, Helios Nanolab 600). The thermal stability of the polymer was evaluated by thermogravimetric analysis (TG-DTA, SDT Q600).

4.5. Catalytic reduction of nitrocompounds

All the catalytic reactions were performed with magnetic stirring (600 rpm). In a typical procedure, 100 mL of an aqueous solution consisting of 4 μmol 4-NP and 0.70 μmol $NaBH_4$ was added into a beaker along with 5.0 mg of catalyst sample under vigorous stirring. At predetermined time intervals, approximately 3 mL of 4-NP solution was withdrawn and measured using an ultraviolet-visible (UV-vis) spectrophotometer (Cary 5000, Agilent, USA) to record the change in scanning range of 200–500 nm for 4-NP and 200–350 for nitrobenzene derivatives at room temperature. The reusability of the catalyst was investigated by directly removing the catalyst from the solution after the reaction and drying for 1 h. The catalytic reduction of the nitro compounds was performed under the same conditions of 4-NP. The catalytic efficiency (η) would be defined as,

$$\eta = \frac{A_0 - A_t}{A_0} \times 100\% \quad (3)$$

where A_0 is the initial concentration of 4-NP and A_t is the concentration of 4-NP at a certain time during the catalytic reaction.

4.6. Computational calculation by density functional theory (DFT)

Calculations of frontier molecular orbitals of 4-NP and 4-AP compounds were performed using the Gaussian 09 W package using density functional theory (DFT) at the B3LYP level with the 6-31G++(d,p) basis set. The polarizable continuum model was adapted in order to account for the effects of aqueous solvation implicitly. We calculated the energies of frontier molecular orbitals, such as the highest occupied molecular orbital (HOMO) as well as the lowest unoccupied molecular orbital (LUMO).

The simulation for the Cu-PVAc@MgO system is as follows: we performed SCC DFTB-MD using the *x*TB method as implemented in the DFTB+ software, version 22.1. Our system consisted of Cu nanoparticles on a MgO substrate surrounded by 30 polymer chains. To ensure adequate spacing between periodic images of the nanoparticles, we chose a simulation cell with at least 40 Å between them. This design choice allows for a high virtual concentration of nanoparticles while maintaining separation between slabs, a common practice in DFT simulations. Additionally, we leveraged the XLBOMD scheme, as implemented in DFTB+, to accelerate the SCC convergence of the system. Dispersion correction (D4) was to take van der Waals forces into account. The system was equilibrated at a temperature of 300 K for 1000 steps of 1.0 fs in the NVT ensemble using SCC DFTB-MD. This was followed by a data gathering simulation of 4000 steps of 1.0 fs in the NVE ensemble using SCC DFTB-MD. Finally, the obtained structures were optimized using the conjugate gradient method. In order to determine the possible adsorption sites of 4-NP on the obtained structures, 5 NB molecules were randomly added to each optimized unit cell. Likewise, A 5ps DFTB MD simulation was performed starting at temperatures of 300 K with a step size of 0.5 fs. The adsorption energy is calculated as follows:

$$\Delta E_{\text{adsorption}} = E_{\text{surface/adsorbant}} - E_{\text{surface}} - E_{\text{adsorbant}} \quad (4)$$

Author contributions

Rosy Amalia Kurnia Putri: conceptualization, methodology, investigation, data curation, visualization, writing – original draft, writing – review and editing. Wail Al Zoubi: conceptualization, validation, supervision, writing – review and editing, project administration. Bassem Assfour: data curation and DFT calculation. Abdul Wahab Allaf: data curation and DFT calculation. Sudiyarmanto: writing – review and editing. Young Gun Ko: supervision, funding acquisition.

Data availability

The raw/processed data required to reproduce these findings cannot be shared at this time as the data also forms part of an ongoing study.

Conflicts of interest

The authors declare no competing interests.

Acknowledgements

This work is supported by the National Research Foundation (NRF) of South Korea (NRF-2022R1A2C1004392).

References

1 Z. Gao, S. Shao, W. Gao, D. Tang, D. Tang, S. Zou, M. J. Kim and X. Xia, Morphology-Invariant Metallic Nanoparticles

with Tunable Plasmonic Properties, *ACS Nano*, 2021, **15**, 2428–2438, DOI: **10.1021/acsnano.0c06123**.

2 Y. Liu, C. H. Liu, T. Debnath, Y. Wang, D. Pohl, L. V. Besteiro, D. M. Meira, S. Huang, F. Yang, B. Rellinghaus, M. Chaker, D. F. Perepichka and D. Ma, Silver nanoparticle enhanced metal-organic matrix with interface-engineering for efficient photocatalytic hydrogen evolution, *Nat. Commun.*, 2023, **14**, 1–12, DOI: **10.1038/s41467-023-35981-8**.

3 T. W. van Deelen, C. Hernández Mejía and K. P. de Jong, Control of metal-support interactions in heterogeneous catalysts to enhance activity and selectivity, *Nat. Catal.*, 2019, **2**, 955–970, DOI: **10.1038/s41929-019-0364-x**.

4 J. Yu, X. Sun, X. Tong, J. Zhang, J. Li, S. Li, Y. Liu, N. Tsubaki, T. Abe and J. Sun, Ultra-high thermal stability of sputtering reconstructed Cu-based catalysts, *Nat. Commun.*, 2021, **12**, 1–10, DOI: **10.1038/s41467-021-27557-1**.

5 J. Guo, Y. Zhang, L. Shi, Y. Zhu, M. F. Mideksa, K. Hou, W. Zhao, D. Wang, M. Zhao, X. Zhang, J. Lv, J. Zhang, X. Wang and Z. Tang, Boosting Hot Electrons in Hetero-superstructures for Plasmon-Enhanced Catalysis, *J. Am. Chem. Soc.*, 2017, **139**, 17964–17972, DOI: **10.1021/jacs.7b08903**.

6 X. Kong, B. Liu, Z. Tong, R. Bao, J. Yi, S. Bu, Y. Liu, P. Wang, C. S. Lee and W. Zhang, Charge-switchable ligand ameliorated cobalt polyphthalocyanine polymers for high-current-density electrocatalytic CO2 reduction, *SmartMat*, 2024, 1–11, DOI: **10.1002/smm2.1262**.

7 J. Tian, J. Li, Y. Guo, Z. Liu, B. Liu and J. Li, Oxygen vacancy mediated bismuth-based photocatalysts, *Adv. Powder Mater.*, 2024, **3**, 100201, DOI: **10.1016/j.apmate.2024.100201**.

8 S. Li, C. You, K. Rong, C. Zhuang, X. Chen and B. Zhang, Chemically bonded Mn0.5Cd0.5S/BiOBr S-scheme photocatalyst with rich oxygen vacancies for improved photocatalytic decontamination performance, *Adv. Powder Mater.*, 2024, **3**, 100183, DOI: **10.1016/j.apmate.2024.100183**.

9 B. Huang, X. Fu, K. Wang, L. Wang, H. Zhang, Z. Liu, B. Liu and J. Li, Chemically bonded BiVO4/Bi19Cl3S27 heterojunction with fast hole extraction dynamics for continuous CO2 photoreduction, *Adv. Powder Mater.*, 2024, **3**, 100140, DOI: **10.1016/j.apmate.2023.100140**.

10 Y. Ai, M. Q. He, H. Sun, X. Jia, L. Wu, X. Zhang, H. bin Sun and Q. Liang, Ultra-Small High-Entropy Alloy Nanoparticles: Efficient Nanozyme for Enhancing Tumor Photothermal Therapy, *Adv. Mater.*, 2023, **35**, 1–13, DOI: **10.1002/adma.202302335**.

11 Y. Ai, Z. Hu, L. Liu, J. Zhou, Y. Long, J. Li, M. Ding, H. Bin Sun and Q. Liang, Magnetically Hollow Pt Nanocages with Ultrathin Walls as a Highly Integrated Nanoreactor for Catalytic Transfer Hydrogenation Reaction, *Adv. Sci.*, 2019, **6**, 1802132, DOI: **10.1002/advs.201802132**.

12 Y. Ai, M. He, F. Zhang, Y. Long, Y. Li, Q. Han, M. Ding, H. Bin Sun and Q. Liang, Metallo-supramolecular polymer engineered porous carbon framework encapsulated stable ultra-small nanoparticles: A general approach to construct highly dispersed catalysts, *J. Mater. Chem. A*, 2018, **6**, 16680–16689, DOI: **10.1039/c8ta05369c**.

13 Y. Xiong, Y. Lin, X. Wang, Y. Zhao and J. Tian, Defect engineering on SnO2 nanomaterials for enhanced gas sensing performances, *Adv. Powder Mater.*, 2022, **1**, 100033, DOI: **10.1016/j.apmate.2022.02.001**.

14 J. Ye, B. Zhu, B. Cheng, C. Jiang, S. Wageh, A. A. Al-Ghamdi and J. Yu, Synergy between Platinum and Gold Nanoparticles in Oxygen Activation for Enhanced Room-Temperature Formaldehyde Oxidation, *Adv. Funct. Mater.*, 2022, **32**, 2110423, DOI: **10.1002/adfm.202110423**.

15 E. K. Dann, E. K. Gibson, R. H. Blackmore, C. R. A. Catlow, P. Collier, A. Chutia, T. E. Erden, C. Hardacre, A. Kroner, M. Nachtegaal, A. Raj, S. M. Rogers, S. F. R. Taylor, P. Thompson, G. F. Tierney, C. D. Zeinalipour-Yazdi, A. Goguet and P. P. Wells, Structural selectivity of supported Pd nanoparticles for catalytic NH 3 oxidation resolved using combined operando spectroscopy, *Nat. Catal.*, 2019, **2**, 157–163, DOI: **10.1038/s41929-018-0213-3**.

16 L. Y. Zhang, T. Zeng, L. Zheng, Y. Wang, W. Yuan, M. Niu, C. X. Guo, D. Cao and C. M. Li, Epitaxial growth of Pt–Pd bimetallic heterostructures for the oxygen reduction reaction, *Adv. Powder Mater.*, 2023, **2**, 100131, DOI: **10.1016/j.apmate.2023.100131**.

17 N. K. Ojha, G. V. Zyryanov, A. Majee, V. N. Charushin, O. N. Chupakhin and S. Santra, Copper nanoparticles as inexpensive and efficient catalyst: A valuable contribution in organic synthesis, *Coord. Chem. Rev.*, 2017, **353**, 1–57, DOI: **10.1016/j.ccr.2017.10.004**.

18 P. Song, Y. Lei, X. Hu, C. Wang, J. Wang and Y. Tang, Rapid one-step synthesis of carbon-supported platinum–copper nanoparticles with enhanced electrocatalytic activity via microwave-assisted heating, *J. Colloid Interface Sci.*, 2020, **574**, 421–429, DOI: **10.1016/j.jcis.2020.04.041**.

19 W. Ma, S. Xie, T. Liu, Q. Fan, J. Ye, F. Sun, Z. Jiang, Q. Zhang, J. Cheng and Y. Wang, Electrocatalytic reduction of CO2 to ethylene and ethanol through hydrogen-assisted C–C coupling over fluorine-modified copper, *Nat. Catal.*, 2020, **3**, 478–487, DOI: **10.1038/s41929-020-0450-0**.

20 M. Wu, C. Zhu, K. Wang, G. Li, X. Dong, Y. Song, J. Xue, W. Chen, W. Wei and Y. Sun, Promotion of CO2 Electrochemical Reduction via Cu Nanodendrites, *ACS Appl. Mater. Interfaces*, 2020, **12**, 11562–11569, DOI: **10.1021/acsami.9b21153**.

21 H. Yokota, M. Kadowaki, T. Matsuura, H. Imanaka, N. Ishida and K. Imamura, The Use of a Combination of a Sugar and Surfactant to Stabilize Au Nanoparticle Dispersion against Aggregation during Freeze-Drying, *Langmuir*, 2020, **36**, 6698–6705, DOI: **10.1021/acs.Langmuir.0c00695**.

22 J. Hou, Y. Wang, J. Liu, J. Zhao, S. Long and J. Hao, Enhanced thermal conductivity of copper-doped polyethylene glycol/urchin-like porous titanium dioxide phase change materials for thermal energy storage, *Int. J. Energy Res.*, 2020, **44**, 1909–1919, DOI: **10.1002/er.5045**.

23 L. Wei, Y. Song, P. Liu and X. Kang, Polystyrene nanofibers capped with copper nanoparticles for selective extraction of glutathione prior to its determination by HPLC, *Microchim. Acta*, 2018, **185**, 1–8, DOI: **10.1007/s00604-018-2845-z**.

24 J. Wang, X. Zhao, F. Tang, Y. Li, Y. Yan and L. Li, Synthesis of copper nanoparticles with controllable crystallinity and

their photothermal property, *Colloids Surf., A*, 2021, **626**, 126970, DOI: 10.1016/j.colsurfa.2021.126970.

25 R. Poupart, B. Le Droumaguet, M. Guerrouache and B. Carbonnier, Copper nanoparticles supported on permeable monolith with carboxylic acid surface functionality: Stability and catalytic properties under reductive conditions, *Mater. Chem. Phys.*, 2015, **163**, 446–452, DOI: 10.1016/j.matchemphys.2015.07.064.

26 X. Q. Zhang, R. F. Shen, X. J. Guo, X. Yan, Y. Chen, J. T. Hu and W. Zhong Lang, Bimetallic Ag-Cu nanoparticles anchored on polypropylene (PP) nonwoven fabrics: Superb catalytic efficiency and stability in 4-nitrophenol reduction, *Chem. Eng. J.*, 2021, **408**, 128018, DOI: 10.1016/j.cej.2020.128018.

27 S. Haider, T. Kamal, S. B. Khan, M. Omer, A. Haider, F. U. Khan and A. M. Asiri, Natural polymers supported copper nanoparticles for pollutants degradation, *Appl. Surf. Sci.*, 2016, **387**, 1154–1161, DOI: 10.1016/j.apsusc.2016.06.133.

28 X. Sun, P. He, Z. Gao, Y. Liao, S. Weng, Z. Zhao, H. Song and Z. Zhao, Multi-crystalline N-doped Cu/CuxO/C foam catalyst derived from alkaline N-coordinated HKUST-1/CMC for enhanced 4-nitrophenol reduction, *J. Colloid Interface Sci.*, 2019, **553**, 1–13, DOI: 10.1016/j.jcis.2019.06.004.

29 L. Wang, N. Gao, F. Han, Y. Mao and J. Tian, Immobilization of nano-Cu on ceramic membrane by dopamine assisted flowing synthesis for enhanced catalysis, *Sep. Purif. Technol.*, 2023, **326**, 124781, DOI: 10.1016/j.seppur.2023.124781.

30 A. D. Verma, R. K. Mandal and I. Sinha, Kinetics of p-nitrophenol reduction catalyzed by PVP stabilized copper nanoparticles, *Catal. Lett.*, 2015, **145**, 1885–1892, DOI: 10.1007/s10562-015-1605-5.

31 P. Mohammed Yusuf Ansari, R. M. Muthukrishnan, C. Vedhi, K. Sakthipandi and S. M. Abdul Kader, Novel approach for green synthesis of Cu-NPs using Centella asiatica leaf extract, assisted by BiFeO3 nanoparticles for electrochemical glucose- and fructose-sensing applications, *Inorg. Chem. Commun.*, 2023, **158**, 111669, DOI: 10.1016/j.inoche.2023.111669.

32 H. O. Lee, A. M. Vallejos, J. M. Rimsza, C. D. W. Chin, M. Ringgold, J. R. Nicholas and L. R. J. Treadwell, Understanding the effects of polar and non-polar surfactants on the oxidation performance of copper nanoparticles, *J. Mater. Sci.*, 2022, **57**, 6167–6181, DOI: 10.1007/s10853-022-07021-1.

33 S. C. Mali, A. Dhaka, C. K. Githala and R. Trivedi, Green synthesis of copper nanoparticles using Celastrus paniculatus Willd. leaf extract and their photocatalytic and antifungal properties, *Biotechnol. Rep.*, 2020, **27**, e00518, DOI: 10.1016/j.btre.2020.e00518.

34 M. J. Islam, M. Granollers Mesa, A. Osatiashtiani, M. J. Taylor, J. C. Manayil, C. M. A. Parlett, M. A. Isaacs and G. Kyriakou, The effect of metal precursor on copper phase dispersion and nanoparticle formation for the catalytic transformations of furfural, *Appl. Catal., B*, 2020, **273**, 119062, DOI: 10.1016/j.apcatb.2020.119062.

35 R. Shokry, H. M. Abd El Salam, D. Aman, S. Mikhail, T. Zaki, W. M. A. El Rouby, A. A. Farghali, W. Al Zoubi and Y. G. Ko, MOF-derived core–shell MnO@Cu/C as high-efficiency catalyst for reduction of nitroarenes, *Chem. Eng. J.*, 2023, **459**, 141554, DOI: 10.1016/j.cej.2023.141554.

36 L. Jin, G. He, J. Xue, T. Xu and H. Chen, Cu/graphene with high catalytic activity prepared by glucose blowing for reduction of p-nitrophenol, *J. Cleaner Prod.*, 2017, **161**, 655–662, DOI: 10.1016/j.jclepro.2017.05.162.

37 K. Sasikumar, R. Rajamanikandan and H. Ju, Inner filter effect-based highly sensitive quantification of 4-nitrophenol by strong fluorescent N, S co-doped carbon dots, *Carbon Lett.*, 2024, **34**, 851–863, DOI: 10.1007/s42823-023-00666-1.

38 J. Im, Y. Liu, Q. Hu, G. F. Trindade, C. Parmenter, M. Fay, Y. He, D. J. Irvine, C. Tuck, R. D. Wildman, R. Hague and L. Turyanska, Strategies for Integrating Metal Nanoparticles with Two-Photon Polymerization Process: Toward High Resolution Functional Additive Manufacturing, *Adv. Funct. Mater.*, 2023, **33**, 1–9, DOI: 10.1002/adfm.202211920.

39 M. P. Kamil, T. Suhartono and Y. G. Ko, Corrosion behavior of plasma electrolysis layer cross-linked with a conductive polymer coating, *J. Mater. Res. Technol.*, 2021, **15**, 4672–4682, DOI: 10.1016/j.jmrt.2021.10.090.

40 R. A. K. Putri, N. Nashrah, D. I. Han, W. Al Zoubi and Y. G. Ko, Chemical incorporation of Mn3O4 into TiO2 coating by benzotriazole working as electron donor: Electrochemical and catalytic performance, *Composites, Part B*, 2022, **232**, 109609, DOI: 10.1016/j.compositesb.2021.109609.

41 J. Liu, R. Ye, J. Shi, H. Wang, L. Wang, P. Jian and D. Wang, Construction of Cu nanoparticles embedded nitrogen–doped carbon derived from biomass for highly boosting the nitrobenzene reduction: An experimental and theoretical understanding, *Chem. Eng. J.*, 2021, **419**, 129640, DOI: 10.1016/j.cej.2021.129640.

42 A. Paajanen, J. Vaari and T. Verho, Crystallization of cross-linked polyethylene by molecular dynamics simulation, *Polymer*, 2019, **171**, 80–86, DOI: 10.1016/j.polymer.2019.03.040.

43 S. Kundu, L. Ma, W. Dai, Y. Chen, A. M. Sinyukov and H. Liang, Polymer Encapsulated Self-Assemblies of Ultrasmall Rhenium Nanoparticles: Catalysis and SERS Applications, *ACS Sustainable Chem. Eng.*, 2017, **5**, 10186–10198, DOI: 10.1021/acssuschemeng.7b02175.

44 S. Hu, M. Huang, J. Li, J. He, K. Xu, X. Rao, D. Cai and G. Zhan, Tailoring the electronic states of Pt by atomic layer deposition of Al2O3 for enhanced CO oxidation performance: Experimental and theoretical investigations, *Appl. Catal., B*, 2023, **333**, 122804, DOI: 10.1016/j.apcatb.2023.122804.

45 G. Acik, C. E. Cansoy and M. Kamaci, Effect of flow rate on wetting and optical properties of electrospun poly(vinyl acetate) micro-fibers, *Colloid Polym. Sci.*, 2019, **297**, 77–83, DOI: 10.1007/s00396-018-4443-3.

46 X. Liu, D. Gregurec, J. Irigoyen, A. Martinez, S. Moya, R. Ciganda, P. Hermange, J. Ruiz and D. Astruc, Precise localization of metal nanoparticles in dendrimer nanosnakes or inner periphery and consequences in catalysis, *Nat. Commun.*, 2016, **7**, 1–8, DOI: 10.1038/ncomms13152.

47 A. Samide, B. Tutunaru, C. Merişanu and N. Cioateră, Thermal analysis: an effective characterization method of polyvinyl acetate films applied in corrosion inhibition field,

J. Therm. Anal. Calorim., 2020, **142**, 1825–1834, DOI: 10.1007/s10973-020-09489-y.

48 J. Zhang, C. Zhao, C. Li, S. Li, C. W. Tsang and C. Liang, The role of oxophilic Mo species in Pt/MgO catalysts as extremely active sites for enhanced hydrodeoxygenation of dibenzofuran, *Catal. Sci. Technol.*, 2020, **10**, 2948–2960, DOI: 10.1039/d0cy00341g.

49 S. Ji, Y. Chen, G. Zhao, Y. Wang, W. Sun, Z. Zhang, Y. Lu and D. Wang, Atomic-level insights into the steric hindrance effect of single-atom Pd catalyst to boost the synthesis of dimethyl carbonate, *Appl. Catal., B*, 2022, **304**, 120922, DOI: 10.1016/j.apcatb.2021.120922.

50 W. Al Zoubi, N. Nashrah, R. A. K. Putri, A. W. Allaf, B. Assfour and Y. G. Ko, Strong dual-metal-support interactions induced by low-temperature plasma phenomenon, *Mater. Today Nano*, 2022, **18**, 100213, DOI: 10.1016/j.mtnano.2022.100213.

51 J. Liu, R. Ye, J. Shi, H. Wang, L. Wang, P. Jian and D. Wang, Construction of Cu nanoparticles embedded nitrogen–doped carbon derived from biomass for highly boosting the nitrobenzene reduction: An experimental and theoretical understanding, *Chem. Eng. J.*, 2021, **419**, 129640, DOI: 10.1016/j.cej.2021.129640.

52 Y. Li, H. Xu and G. Zhang, Porous carbon-encapsulated CuxO/Cu catalyst derived from N-coordinated MOF for ultrafast 4-nitrophenol reduction in batch and continuous flow reactors, *J. Environ. Chem. Eng.*, 2022, **10**, 108677, DOI: 10.1016/j.jece.2022.108677.

53 P. Huang, R. Baldenhofer, R. P. Martinho, L. Lefferts and J. A. Faria Albanese, Stimulus-Responsive Control of Transition States on Nanohybrid Polymer-Metal Catalysts, *ACS Catal.*, 2023, 6590–6602, DOI: 10.1021/acscatal.3c00276.

54 M. Kohantorabi and M. R. Gholami, Kinetic Analysis of the Reduction of 4-Nitrophenol Catalyzed by CeO2 Nanorods-Supported CuNi Nanoparticles, *Ind. Eng. Chem. Res.*, 2017, **56**, 1159–1167, DOI: 10.1021/acs.iecr.6b04208.

55 K. Kuroda, T. Ishida and M. Haruta, Reduction of 4-nitrophenol to 4-aminophenol over Au nanoparticles deposited on PMMA, *J. Mol. Catal. A: Chem.*, 2009, **298**, 7–11, DOI: 10.1016/j.molcata.2008.09.009.

56 Z. M. El-Bahy, Preparation and characterization of Pt-promoted NiY and CoY catalysts employed for 4-nitrophenol reduction, *Appl. Catal., A*, 2013, **468**, 175–183, DOI: 10.1016/j.apcata.2013.08.047.

57 J. R. Chiou, B. H. Lai, K. C. Hsu and D. H. Chen, One-pot green synthesis of silver/iron oxide composite nanoparticles for 4-nitrophenol reduction, *Dalton Trans.*, 2013, **248–249**, 394–400, DOI: 10.1016/j.jhazmat.2013.01.030.

58 M. Bagheri, A. Melillo, B. Ferrer, M. Y. Masoomi and H. Garcia, Quasi-HKUST Prepared via Postsynthetic Defect Engineering for Highly Improved Catalytic Conversion of 4-Nitrophenol, *ACS Appl. Mater. Interfaces*, 2022, **14**, 978–989, DOI: 10.1021/acsami.1c19862.

59 S. Mourdikoudis, V. Montes-García, S. Rodal-Cedeira, N. Winckelmans, I. Pérez-Juste, H. Wu, S. Bals, J. Pérez-Juste and I. Pastoriza-Santos, Highly porous palladium nanodendrites: Wet-chemical synthesis, electron tomography and catalytic activity, *Dalton Trans.*, 2019, **48**, 3758–3767, DOI: 10.1039/c9dt00107g.

60 X. Du, Y. Huang, X. Pan, B. Han, Y. Su, Q. Jiang, M. Li, H. Tang, G. Li and B. Qiao, Size-dependent strong metal-support interaction in TiO2 supported Au nanocatalysts, *Nat. Commun.*, 2020, **11**, 1–8, DOI: 10.1038/s41467-020-19484-4.

61 Z. Huang, Y. Yao, Z. Pang, Y. Yuan, T. Li, K. He, X. Hu, J. Cheng, W. Yao, Y. Liu, A. Nie, S. Sharifi-Asl, M. Cheng, B. Song, K. Amine, J. Lu, T. Li, L. Hu and R. Shahbazian-Yassar, Direct observation of the formation and stabilization of metallic nanoparticles on carbon supports, *Nat. Commun.*, 2020, **11**, 1–9, DOI: 10.1038/s41467-020-20084-5.

62 Y. Zhang, X. Su, L. Li, H. Qi, C. Yang, W. Liu, X. Pan, X. Liu, X. Yang, Y. Huang and T. Zhang, Ru/TiO2Catalysts with Size-Dependent Metal/Support Interaction for Tunable Reactivity in Fischer-Tropsch Synthesis, *ACS Catal.*, 2020, **10**, 12967–12975, DOI: 10.1021/acscatal.0c02780.

63 C. Van Nguyen, S. Lee, Y. G. Chung, W. H. Chiang and K. C. W. Wu, Synergistic effect of metal-organic framework-derived boron and nitrogen heteroatom-doped three-dimensional porous carbons for precious-metal-free catalytic reduction of nitroarenes, *Appl. Catal., B*, 2019, **257**, 117888, DOI: 10.1016/j.apcatb.2019.117888.

64 S. Xu, H. Li, L. Wang, Q. Yue, R. Li, Q. Xue, Y. Zhang and J. Liu, Synthesis of Carbon-Encapsulated Cu-Ag Dimetallic Nanoparticles and Their Recyclable Superior Catalytic Activity towards 4-Nitrophenol Reduction, *Eur. J. Inorg. Chem.*, 2015, 4731–4736, DOI: 10.1002/ejic.201500599.

65 T. W. Kim, M. Kim, S. K. Kim, Y. N. Choi, M. Jung, H. Oh and Y. W. Suh, Remarkably fast low-temperature hydrogen storage into aromatic benzyltoluenes over MgO-supported Ru nanoparticles with homolytic and heterolytic H2 adsorption, *Appl. Catal., B*, 2021, **286**, 119889, DOI: 10.1016/j.apcatb.2021.119889.

66 M. Hu, X. Yan, X. Hu, J. Zhang, R. Feng and M. Zhou, Ultra-high adsorption capacity of MgO/SiO2 composites with rough surfaces for Congo red removal from water, *J. Colloid Interface Sci.*, 2018, **510**, 111–117, DOI: 10.1016/j.jcis.2017.09.063.

67 A. K. Sasmal, S. Dutta and T. Pal, A ternary Cu2O-Cu-CuO nanocomposite: A catalyst with intriguing activity, *Dalton Trans.*, 2016, **45**, 3139–3150, DOI: 10.1039/c5dt03859f.

68 B. Jin, S. Li and X. Liang, Enhanced activity and stability of MgO-promoted Ni/Al2O3 catalyst for dry reforming of methane: Role of MgO, *Fuel*, 2021, **284**, 119082, DOI: 10.1016/j.fuel.2020.119082.

69 E. A. Elkhalifa and H. B. Friedrich, Magnesium oxide as a catalyst for the dehydrogenation of n-octane, *Arabian J. Chem.*, 2018, **11**, 1154–1159, DOI: 10.1016/j.arabjc.2014.10.002.

70 P. Zhao, X. Feng, D. Huang, G. Yang and D. Astruc, Basic concepts and recent advances in nitrophenol reduction by gold- and other transition metal nanoparticles, *Coord. Chem. Rev.*, 2015, **287**, 114–136, DOI: 10.1016/j.ccr.2015.01.002.

71 L. Liu, R. Chen, W. Liu, J. Wu and D. Gao, Catalytic reduction of 4-nitrophenol over Ni-Pd nanodimers supported on nitrogen-doped reduced graphene oxide, *J. Hazard. Mater.*, 2016, **320**, 96–104, DOI: **10.1016/j.jhazmat.2016.08.019**.

72 H. Dan, Y. Song, Y. Xu, Y. Gao, W. Kong, Y. Huang, Q. Yue and B. Gao, Green synthesis of Cu nanoparticles supported on straw-graphene composite for catalytic reduction of p-nitrophenol, *J. Cleaner Prod.*, 2021, **283**, 124578, DOI: **10.1016/j.jclepro.2020.124578**.

73 S. Aslam, F. Subhan, M. Waqas, Y. Zifeng, M. Yaseen and M. Naeem, Cu nanoparticles confined within ZSM-5 derived mesoporous silica (MZ) with enhanced stability for catalytic hydrogenation of 4-nitrophenol and degradation of azo dye, *Microporous Mesoporous Mater.*, 2023, **354**, 112547, DOI: **10.1016/j.micromeso.2023.112547**.

74 M. Rajabzadeh, H. Eshghi, R. Khalifeh and M. Bakavoli, Generation of Cu nanoparticles on novel designed Fe3O4@-SiO2/EP.EN.EG as reusable nanocatalyst for the reduction of nitro compounds, *RSC Adv.*, 2016, **6**, 19331–19340, DOI: **10.1039/c5ra26020e**.

75 F. Wang, F. Pan, G. Li, P. Zhang and N. Wang, Construction of spherical montmorillonite supported Cu-based catalyst doping with a covalent organic framework for 4-nitrophenol removal, *Appl. Clay Sci.*, 2021, **214**, 106278, DOI: **10.1016/j.clay.2021.106278**.

76 T. Kamal, A. M. Asiri and N. Ali, Catalytic reduction of 4-nitrophenol and methylene blue pollutants in water by copper and nickel nanoparticles decorated polymer sponges, *Spectrochim. Acta, Part A*, 2021, **261**, 120019, DOI: **10.1016/j.saa.2021.120019**.

77 T. Yang, Y. Tang, L. Liu, Y. Gao and Y. Zhang, Cu-anchored CNTs for effectively catalytic reduction of 4-nitrophenol, *Chem. Phys.*, 2020, **533**, 110738, DOI: **10.1016/j.chemphys.2020.110738**.

78 P. Deka, R. C. Deka and P. Bharali, In situ generated copper nanoparticle catalyzed reduction of 4-nitrophenol, *New J. Chem.*, 2014, **38**, 1789–1793, DOI: **10.1039/c3nj01589k**.

79 S. Oh, H. Yu, Y. Han, H. S. Jeong and H. J. Hong, 3-D porous cellulose nanofibril aerogels with a controllable copper nanoparticle loading as a highly efficient non-noble-metal catalyst for 4-nitrophenol reduction, *Chemosphere*, 2022, **301**, 134518, DOI: **10.1016/j.chemosphere.2022.134518**.

80 W. L. Tan, N. H. H. Abu Bakar and M. Abu Bakar, Catalytic reduction of p-nitrophenol using chitosan stabilized copper nanoparticles, *Catal. Lett.*, 2015, **145**, 1626–1633, DOI: **10.1007/s10562-015-1547-y**.

81 A. N. Alqhobisi, M. S. Alhumaimess, I. H. Alsohaimi, H. M. A. Hassan, A. A. Essawy, M. R. El-Aassar and H. Kalil, Efficient nitrophenol reduction with Noria-GO nanocomposite decorated with Pd–Cu nanoparticles, *Environ. Res.*, 2023, **231**, 116259, DOI: **10.1016/j.envres.2023.116259**.

82 W. Al Zoubi, A. W. Allaf, B. Assfour and Y. G. Ko, Concurrent Oxidation-Reduction Reactions in a Single System Using a Low-Plasma Phenomenon: Excellent Catalytic Performance and Stability in the Hydrogenation Reaction, *ACS Appl. Mater. Interfaces*, 2022, **14**, 6740–6753, DOI: **10.1021/acsami.1c22192**.

83 J. Polte, Fundamental growth principles of colloidal metal nanoparticles - a new perspective, *CrystEngComm*, 2015, **17**, 6809–6830, DOI: **10.1039/c5ce01014d**.

